Proceedings of the Twelfth International Conference on
Engineering Computational Technology
Edited by: P. Iványi, J. Kruis and B.H.V. Topping
Civil-Comp Conferences, Volume 8, Paper 6.1
Civil-Comp Press, Edinburgh, United Kingdom, 2024
ISSN: 2753-3239, doi: 10.4203/ccc.8.6.1

Simulation of Passenger Car Aerodynamics in Overtaking Manoeuvres with an Adaptive Lattice Boltzmann Method

R. Deiterding[1], J. Harding[1] and M. Grondeau[2]

[1] Department Aeronautics & Astronautics, University of Southampton, Southampton, United Kingdom
[2] Laboratoire Universitaire des Sciences Appliquées de Cherbourg, Université de Caen Normandie, Cherbourg-Octeville, France

Abstract

Using the freely available DriAer passenger car geometries, the benefits of our Cartesian adaptive lattice Boltzmann solver AMROC-LBM for simulating the aerodynamics of vehicles in motion are demonstrated. A large eddy simulation (LES) approach with wall function model is applied to approximate the transient turbulent flow field, while motion is incorporated in a scalable way by representing complex moving bodies with signed distance level set functions and moving wall boundary conditions. The adaptive lattice Boltzmann-LES method in AMROC-LBM is first validated against experimentally measured drag coefficients of a single car geometry. Subsequently, a study of an overtaking manoeuvrer at 25% scale is conducted and verified with previously obtained simulation results from StarCCM+. Finally, predictions for a realistic overtaking manoeuvrer at full scale are presented.

Keywords: CFD, dynamic mesh adaptation, lattice Boltzmann method, large eddy simulation, DrivAer, moving geometries

1 Introduction

Simulating the transient aerodynamic behaviour of road vehicles in relative motion to one another requires a numerical method that is able to represent the turbulent flow fields around complex geometries with high accuracy and, at the same time, is able to accommodate the motion with a suitable meshing approach. Of paramount importance for vehicle aerodynamics is an adequate numerical treatment of the viscous boundary layers that develop over planar surfaces. Finite-volume-based computational fluid dynamics (CFD) codes, that can handle such setups competently, are relatively rare and typically employ geometry-aligned structured boundary-layer meshes around the geometries that can be set in motion by allowing the near-body meshes to slide over a usually unstructured background mesh. Overlapping sub-meshes in this *overset* or *Chimera* approach synchronize respective boundary data within a time step with complex, non-conservative interpolation operations. Imminent ambiguities arise when multiple boundary meshes would be overlapping.

Here, we use Cartesian dynamically adaptive meshes instead that are refined on-the-fly based on geometry motion as well as the turbulent flow field. An advanced lattice Boltzmann method (LBM) with LES sub-grid scale modelling is utilized to approximate the flow field. Correct near-wall boundary layer behaviour is incorporated by a turbulent wall function. All models are implemented in our in-house MPI-parallel Cartesian mesh adaptation framework AMROC. To demonstrate the accuracy of the latest version of our aerodynamics solver AMROC-LBM [1], we predict the drag coefficients of the freely available DriAver car geometries. While other solvers generally struggle to represent the wheels with moving spokes, our dynamically adaptive Cartesian approach easily incorporates this complexity. Finally, two overtaking manoeuvrers of a DrivAer car passing an identical DrivAer geometry are modelled. While the second configuration is in full car scale, the first case serves as verification using a reduced 25% scale and is compared to transient drag predictions from the commercial CFD solver StarCCM+, which employs an overset finite-volume mesh method with static wheel representation.

The paper is organized as follows: In Section 2 the crucial components of the adaptive LBM-LES method of AMROC-LBM are described. Section 3 presents simulation results for single cars, while Section 4 describes the transient results for the two overtaking scenarios. Finally, the conclusions are given in Section 5.

2 Adaptive lattice Boltzmann solver

2.1 Lattice Boltzmann scheme

The lattice Boltzmann method is an instationary weakly-compressible method derived from the lattice gas automata for the discretization of the Boltzmann equation. It describes the fluid behaviour by considering a statistical description of the molecules' behaviour through a distribution function $f(\mathbf{x}, \xi, t)$. The distribution function rep-

resents the probability density of molecules being at a location $\mathbf{x}$, which have the velocity ξ, at time t. The key idea of the LBM approach is to use a finite set of propagation directions to discretize the velocity space and represent the contribution from each discrete unit velocity direction with a discrete partial distribution function $f_\alpha(\mathbf{x}, t)$. Here, all computations are three-dimensional and 27 unit direction vectors $\mathbf{e}_\alpha$ are used, which is referred to as a D3Q27 scheme. As it is most common, our implementation of the LBM is internally on the non-dimensional unit lattice and is split into two steps. The first one is the streaming of each distribution field by exactly one lattice point as specified by the respective unit direction vector, i.e.,

$$\check{f}_\alpha(\mathbf{x}, t) = f_\alpha(\mathbf{x} - \mathbf{e}_\alpha, t). \tag{1}$$

The second step is the collision. Here, the regularized BGK (Bhatnagar-Gross-Krook) collision operator described by Latt and Chopard [2] is used. It reads

$$f_\alpha(\mathbf{x}, t + \Delta t) = \check{f}^{(0)}_\alpha(\mathbf{x}, t) + (1 - \omega)\check{f}^{(1)}_\alpha(\mathbf{x}, t), \tag{2}$$

where ω is the non-dimensional relaxation frequency of the discrete method. The relaxation frequency is related to the kinematic viscosity of the fluid through $\nu = c_s^2 \left(\frac{1}{\omega} - \frac{1}{2}\right) \Delta t$, where the speed of sound $c_s = 340\,\mathrm{m/s}$ has been used for all computations below, and Δt is the physical time step. In Eq. (2), the superscript $\check{}$ represents the post-propagation distribution state. To compute the equilibrium part $f^{(0)}$ and the non-equilibrium part $f^{(1)}_\alpha = f_\alpha - f^{(0)}_\alpha$, the regularized recursive (RR) approach by Malaspinas [3] is applied. The implemented model uses the recursive approach up to order 6 for both equilibrium and non-equilibrium parts. It has been shown that this RR-BGK scheme is stable and accurate at high Reynolds numbers, which makes it suitable for aerodynamics.

In order to evaluate the physical quantities of interest, the non-dimensional distributions on the unit lattice need to be rescaled according to the actual physical time step Δt and the physical grid spacing of the Cartesian mesh Δx, using the lattice speed $c = \Delta x / \Delta t$. In the LBM, the macroscopic variables such as the pressure and velocities are recovered as moments of the distribution functions. The gas density ρ and the velocity vector $\mathbf{u}$ are evaluated by a simple rescaling of the 0th moment and 1st moment of the probability density with a reference density ρ_0 and the lattice speed, respectively. i.e.

$$\rho = \rho_0 \sum_\alpha f_\alpha, \qquad \mathbf{u} = c \sum_\alpha \mathbf{e}_\alpha f_\alpha. \tag{3}$$

The total pressure can be computed from the density as $p = c_s^2(\rho - \rho_0) + p_0$, where $c_s = c\tilde{c}_s$ is the speed of sound and p_0 is the ambient pressure. The lattice speed of sound $\tilde{c}_s$ is equal to $1/\sqrt{3}$ for D3Q27.

2.2 Adaptive mesh refinement

The LBM used here is formulated for an equidistant Cartesian mesh. In order to increase accuracy at a reduced computational cost, a block-structured adaptive mesh

refinement (SAMR) technique is applied [4]. In this approach, cells are clustered into non-overlapping rectangular grids. Each grid has a halo of cells for boundary conditions and synchronization, cf. [4]. The mesh widths of two adjacent levels follow the relation $\Delta x^c/\Delta x^f = \Delta t^c/\Delta t^f = r$, where the superscript f refers to the fine mesh and c refers to the coarse mesh. The simultaneous refinement of spatial and temporal mesh width is fully compatible with the explicit LBM and by formulating the LBM on cell-based data structures, the method can be made to fit smoothly into the recursive SAMR refinement and integration procedure. More details of our implementation of an adaptive LBM within AMROC can be found for instance in [5].

Grids at different levels need to exchange distribution functions at their interface. For fine to coarse transition, distribution functions of fine cells surrounding a coarse cell are averaged. For coarse to fine transition, a spatial and temporal interpolation is used to create the fine distribution functions from surrounding coarse cells, cf. [5]. Distribution functions between levels are further modified by the approach described by Dupuis and Chopard [6], where the non-equilibrium part is rescaled as

$$f_\alpha^c(\mathbf{x},t) = f_\alpha^{f\to c(0)}(\mathbf{x},t) + \frac{r\omega^f}{\omega^c} f_\alpha^{f\to c(1)}(\mathbf{x},t), \tag{4}$$

$$f_\alpha^f(\mathbf{x},t) = f_\alpha^{c\to f(0)}(\mathbf{x},t) + \frac{\omega^c}{r\omega^f} f_\alpha^{c\to f(1)}(\mathbf{x},t), \tag{5}$$

and ω^c and ω^f are the non-dimensional relaxation frequencies of the coarse and fine level, respectively. This approach ensures the continuity in density and velocity, which depends on the equilibrium part, as well as on the strain-rate tensor $\mathbf{S}_{ij}$.

2.3 Large eddy simulation

In order to make turbulent computations at technically relevant Reynolds numbers tractable, the small scales of the turbulent flow are not resolved but modelled with large eddy simulation. The LES model used here is the Smagorinsky model [7]. In this model, the unresolved eddies are represented through an eddy viscosity ν_t that is added to the kinematic viscosity ν. The eddy viscosity is calculated from the filtered strain rate tensor $\overline{\mathbf{S}}_{ij}$ as

$$\nu_t = (C_{sm}\Delta x)^2|\overline{S}|, \tag{6}$$

where the coefficient $C_{sm}(\mathbf{x},t)$ is locally evaluated [8] and $|\overline{S}| = \sqrt{2\overline{\mathbf{S}}_{ij}\overline{\mathbf{S}}_{ij}}$. For the calculation of $\overline{\mathbf{S}}_{ij}$ we have adopted the "consistent strain" approach described by Malaspinas and Sagaut [9]. Since the kinematic viscosity is related to the relaxation frequency, the eddy viscosity is utilized to alter ω locally to

$$\omega^\star = \frac{c_s^2\Delta t}{(\nu+\nu_t) + c_s^2\Delta t/2}. \tag{7}$$

2.4 Boundary conditions

In the SAMR algorithm, it is natural to implement boundary conditions through the use of ghost cells. At the inlet of the numerical domain, we impose the equilibrium distribution functions. They are computed from macroscopic variables ρ and $\mathbf{u}$. The velocity $\mathbf{u}$ is chosen depending on the case. The density ρ is extrapolated from the first fluid cell normal to the boundary. The non-equilibrium is calculated following Guo *et al.* [10] considering $\Delta = 0.5$ as

$$f_\alpha^{(1)}(\mathbf{x}, t) = 0.5 f_\alpha^{(1)}(\mathbf{x} + \mathbf{e}_\alpha, t) + 0.5 f_\alpha^{(1)}(\mathbf{x} + 2\mathbf{e}_\alpha, t). \tag{8}$$

Distribution functions at the outlet of the numerical domain are imposed similarly, except that the density is chosen and the velocity is extrapolated from the first fluid cell. Lateral boundary conditions are also density-imposed boundary conditions.

To prevent outer boundaries from reflecting pressure fluctuations, an absorbing zone as proposed by Kam *et al.* [11] is applied. This absorbing zone is implemented by adding a term $a_\alpha(\mathbf{x}, t)$ to the distribution function during the collision step

$$a_\alpha(\mathbf{x}, t) = -\beta \left(\frac{d_a}{l_a}\right)^2 \left(f_\alpha^{(0)}(\mathbf{x}, t) - f_\alpha^a(\mathbf{x}, t)\right), \tag{9}$$

where d_a is the distance from the inner boundary of the absorbing zone, l_a is the width of the absorbing zone and $f_\alpha^a(\mathbf{x}, t)$ is the equilibrium distribution function computed from the far field density and velocity. β is chosen to be 0.05 [1].

In the AMROC software, non-Cartesian boundaries are represented on the cell-based Cartesian mesh by a scalar level set function that stores the distance to the boundary surface. A fluid cell is treated as an embedded ghost cell if the distance value in the cell center is negative. For computing signed distance functions from triangulated surface meshes, a specially designed algorithm [4] is used.

2.5 Wall function modelling

In realistic aerodynamic configurations the flow forms a turbulent boundary layer around geometries that is very challenging to resolve in numerical simulations. Instead, a wall function model is best used to impose the correct wall-near behaviour as a boundary condition. With y denoting the distance from the wall, u_τ the friction velocity and u the velocity parallel to the wall, the model relates the normalized wall distance $y^+ := u_\tau y/\nu$ and the normalized velocity $u^+ := u/u_\tau$ in the logarithmic law of the wall as $u^+ = \frac{1}{\kappa} \ln y^+ + B$, with empirically obtained constants $\kappa = 0.41$ und $B = 5.3$, which is valid for about $30 < y^+ < 300$. In the viscous sublayer with about $y^+ < 5$ one finds $u^+ = y^+$. Here we use the empirical formula of Musker [12]

$$u^+ = 5.424 \tan^{-1}(0.11976048 y^+ - 0.488023952) + 0.434 \ln\left(\frac{(y^+ 10.6)^{9.6}}{({y^+}^2 - 8.15 y^+ + 86)^2} - 3.50727902\right) \tag{10}$$

that approximates both functions and also includes a smooth transition for the buffer region with $5 < y^+ < 30$.

The use as a boundary condition is depicted in two space dimensions in Fig. 1. For given wall distance y_r, the velocity u parallel to the wall is evaluated from the flow field at the present time step in a reference point, chosen sufficiently far from the wall to allow for unperturbed interpolation from neighbouring lattice points. A Newton method is then used to numerically determine from Eq. (10) the unknown value u_τ. For a ghost cell point at distance y_g from the wall, one uses the obtained value u_τ, to evaluate Eq. (10) at $y_c = -y_g$ to obtain the velocity u' tangential to the wall that is then imposed in the ghost cell point as a moving wall boundary condition. The present implementation further blends the sub-grid scale viscosity ν_t and a wall function eddy viscosity approximation $\nu_{t,y} = \nu\kappa y^+(1-\exp(-y^+/19))^2$ in the wall-near region and the ghost cell as

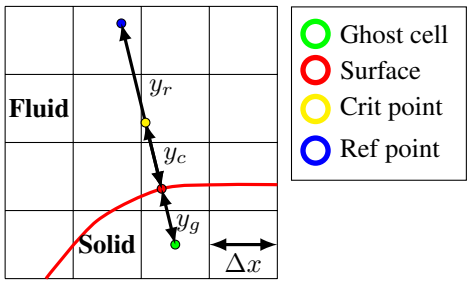

Figure 1: Wall model construction.

$$\nu_t = \begin{cases} \nu_{t,y_c} & , y < y_c, \\ (K^2)\nu_{t,y} + (1-K^2)\nu_t & , y > y_c. \end{cases} \tag{11}$$

2.6 DrivAer geometries

The DrivAer models are freely available car geometries developed by the Technical University of Munich based on the Audi A4 and the BMW 3 series [13]. There are three types of geometries with differences in the shape at the rear of each model, with the *Notchback* and *Fastback* having a smoother change in geometry compared to the *Estateback*. The Estateback is designed for a larger storage capacity in the boot at a cost of additional drag due to the high slant angle [13]. The geometries include wing mirrors, separated detailed or simplified wheels and a smooth or complex floor. Here, the DrivAer models are simulated with a smooth floor, wing mirrors and detailed wheels with spokes. For all simulations, except those in Section 4.1, full-scale car geometries with the reference area $A_0 = 2.16\,\mathrm{m}^2$ are used.

3 Single car results

3.1 Flow field simulation

Full-scale cars are placed in a virtual wind tunnel of extensions $20\,\mathrm{m} \times 12\,\mathrm{m} \times 7\,\mathrm{m}$. An inflow velocity in the x-direction of $u_0 = 16\,\mathrm{m/s}$ is prescribed. Atmospheric conditions of air with $\rho_0 = 1.225\,\mathrm{kg/m^3}$ and $\nu = 1.61{\cdot}10^{-5}\,\mathrm{m^2/s}$ are applied. Moving no-slip wall boundary conditions with velocity u_0 are applied at the bottom of the

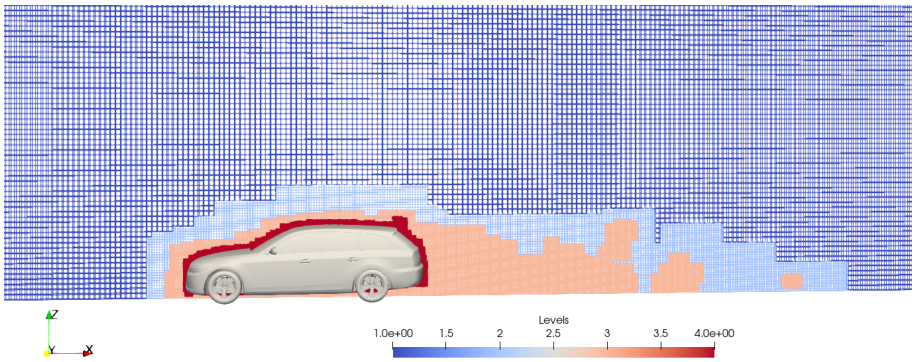

Figure 2: Mesh level in the domain for the most refined Estateback study.

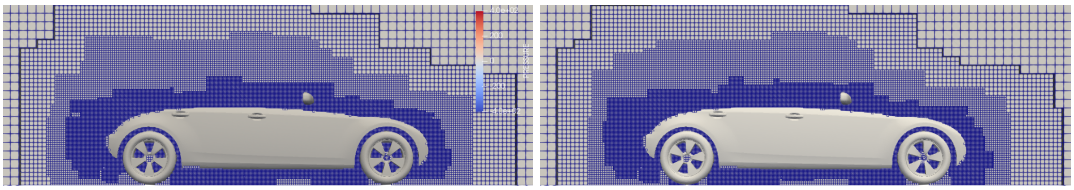

Figure 3: Mesh across the car geometry at $t = 0$ (left) and $t = 0.04157\,\mathrm{s}$ (right). Note the difference in wheel orientation.

domain, while the wall function boundary conditions of Section 2.5 are applied around car body and wheels. A level-0 mesh of resolution $200 \times 120 \times 70$ is used and 2 and 3 additional levels of mesh adaptivity with refinement factor $r = 2$ are used. For convergence assessment a refinement factor of $r = 4$ is also used on the finest level in computations with up to 3 additional levels, giving a finest resolution of $6.25\,\mathrm{mm}$. Simulations are run until a final time $t_e = 2\,\mathrm{s}$, taking ~ 2660 instationary time steps on level 0 and recursively refined steps on higher levels.

Mesh adaptation up to the highest level is based on the geometry. The scaled gradient of the magnitude of the vorticity vector is utilized to refine the wake behind the car up to level 2. A typical snapshot of the dynamically created mesh is shown in Fig. 2. The wheels are set up as rotating with a constant angular velocity corresponding to a velocity of travel of u_0. The AMROC system allows the use of multiple level set functions and here the static car body is represented with one signed distance function and the four rotating wheels with another. Adapting the mesh every 10 level-0 time steps is sufficient to capture the wheel motion. Figure 3 shows the evolving mesh and also how the spoke orientation of the wheels is changing in time.

In Fig. 4 are shown colour plots of the magnitude of the velocity vector averaged over the last second of the computation for all three DrivAer car geometries from the highest resolved computation. In all cases the stagnation point at the front bumper of the car creates a high compressive load. High pressure regions form also in front of the wing mirrors. The flow then accelerates over the roof and separates from the car body for Fastback and Notchback only at the very rear of the boot. In the case of the Estateback flow separation occurs at the rear window and the wake region behind the body is accordingly enlarged. The graphics of Fig. 4 clearly display the influence

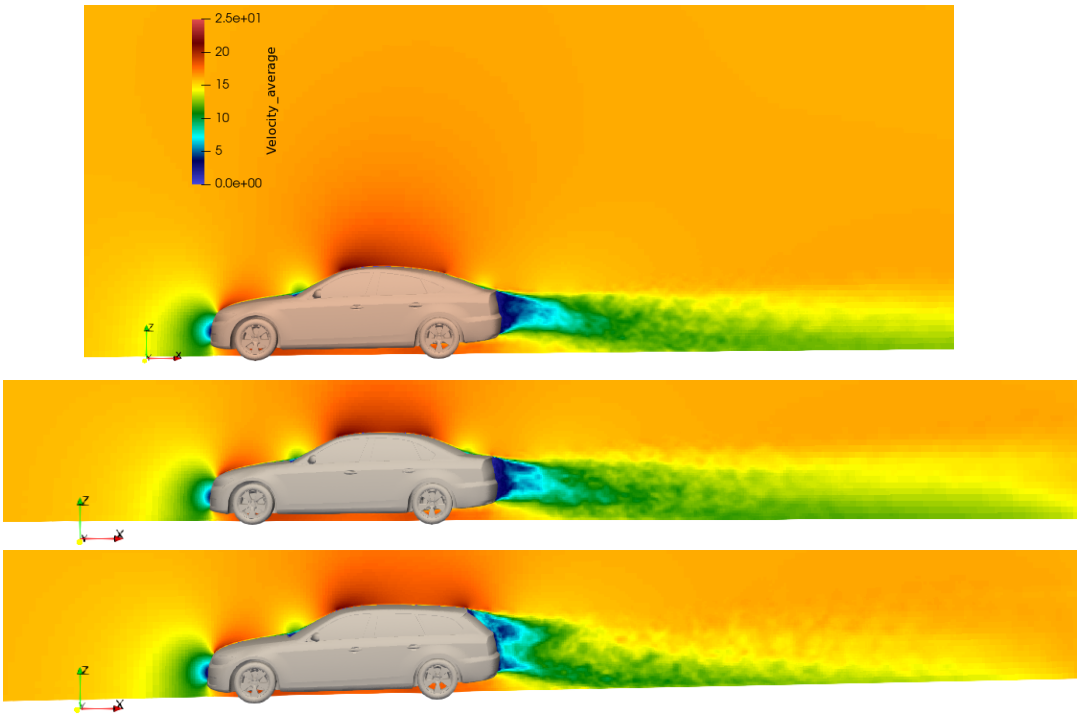

Figure 4: Average velocity field in car mid-plane for the three geometries. Fastback (top), Notchback (middle), Estateback (bottom).

Model	3 levels	4 levels	4 lev, fine	Exp TUM	Exp PVT
Fastback	0.278	0.267	0.267	0.243	0.240
Notchback	0.282	0.272	0.266	0.246	0.246
Estateback	0.322	0.304	0.325	0.292	0.295

Table 1: Comparison of drag coefficient predictions with wind tunnel experiments.

of the boot geometry on the wake formation. Figure 5 shows the average pressure for Notchback and Estateback. The Notchback has a region of high pressure at the bottom of the rear window screen due to the concave corner. This is not the case for the Estateback. The blue regions around the boot of the Estateback model show the regions of very low pressure and adverse pressure gradients from the sharp convex corners, which causes the flow to separate at this point and no longer follow the geometry.

3.2 Drag evaluation

At select time steps, the drag force is integrated over the entire car body. In the LBM, one evaluates 2nd moments of the distribution function and we presently use 1st order interpolation to project the data from the Cartesian lattice points onto the centre of gravity of the surface mesh triangles. Since the flow is highly turbulent, it is of vital importance to use a time-averaged value F_x, in this case over the interval $[1, 2]$ s. The

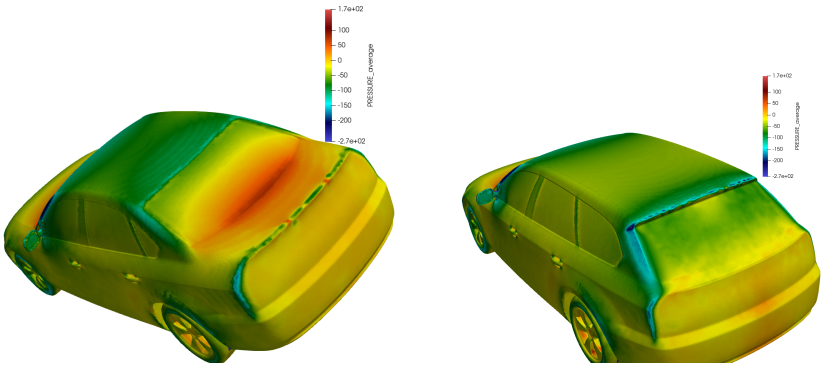

Figure 5: Average pressure at the separation points for the Notchback (left) and Estateback (right) model.

	Pressure		Viscous	
Model	C_D Body	C_D Wheels	C_D Body	C_D Wheels
Fastback	0.1740	0.0894	4.354E-04	9.051E-06
Notchback	0.1779	0.0875	4.356E-04	9.145E-06
Estateback	0.2400	0.0850	4.237E-04	9.173E-06

Table 2: Breakdown of drag coeffient in body and wheel set.

normalized drag coefficient is then computed as $C_D = \dfrac{F_x}{\frac{1}{2}\rho_0 u_0^2 A_0}$.

The drag coefficient predictions using the three different resolution levels are listed in Table 1. Experimental (Exp) wind tunnel data for comparison are from a study by the Technical University Munich (TUM) with data from 40% scale models that included moving ground and moving wheels with the model mounted on stings [13] and a study provided by Ford of Europe (PVT), which used full-scale models in the Volvo wind tunnel. The wheels remained static and the ground was also stationary. The AMROC-LBM runs over-predict the drag by around 8% (Notchback) to 11% (Estateback) compared to the experimental values, however given the moderate resolution used here and the automatic Cartesian meshing approach, this is still deemed satisfactory. Table 2 details how the fine level-4 values break down into the respective car body and the four wheels, divided also into pressure drag and viscous contribution, highlighting the pressure drag dominance.

4 Overtaking simulations

If multiple bodies are in the same flow, their pressure and velocity fields may interact with each other. This change in pressure and velocity in the flow can cause a change in the drag over the body. As the lateral distance between two side-by-side bodies decreases, the drag that the bodies experience increase compared to if they were separate. This is caused by the acceleration of the flow between the two bodies and a

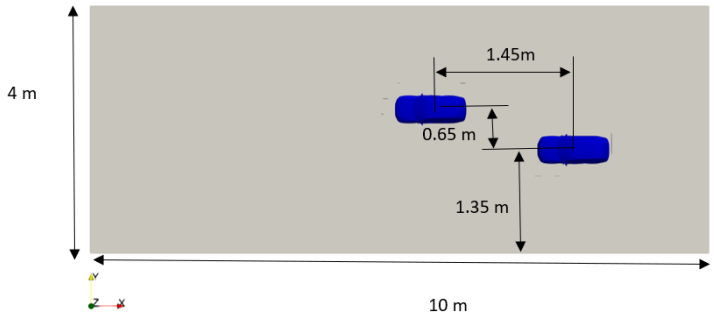

Figure 6: Overhead view of overtaking verification setup.

suction force between the two sides facing each other, known as the Venturi effect. This also results in steeper pressure rises at the rear of the body, creating separation of flow, and increases the drag. Hence, during an overtaking manoeuvrer the drag coefficients of both cars can vary quite significantly. In this section, we simulate two such scenarios involving two identical Estateback models, where one vehicle overtakes the other in adjacent lanes.

4.1 Verification for 25% scale model

To verify the AMROC-LBM solver for multiple moving vehicles, we use a test configuration that we simulated previously in an internship project with the moving overset mesh method in StarCCM+ using the URANS (Unsteady Reynold's Averaged Navier Stokes) modelling approach [14]. The case is set up such that the Estateback model that is initially in front within the domain (Car 1) is static during the simulation with a freestream velocity of $u_0 = 50\,\mathrm{m/s}$. The initially trailing car (Car 2) is moving relative to Car 1 with a relative velocity of $10\,\mathrm{m/s}$ such that it experiences oncoming flow of $60\,\mathrm{m/s}$. The simulation is conducted over a $0.75\,\mathrm{s}$ period as Car 2 passes Car 1. This choice of larger freestream velocity compared to Section 3 allows simulation of a complete overtaking manoeuvrer with considerably fewer time steps. In order to ensure a similar Reynolds number as in Section 3, the geometries are scaled down to $1/4$ size. The used reference area is hence $A_0/16 = 0.135\,\mathrm{m}^2$, while other fluid parameters are as before. Because the wheel motion could not be easily accommodated in StarCCM+, static wheels are also used in the AMROC-LBM simulation.

A sketch of the setup is given in Fig. 6. Car 1 is initially on the left and Car 2 is on the right. Distances relative to a vehicle are measured from the geometrical center of the vehicle and the initial distance is sufficiently large to allow establishment of separate stable drag values. As before, the flow moves in the positive x-direction and Car 2 moves in the negative x-direction. The domain of $10\,\mathrm{m} \times 4\,\mathrm{m} \times 1.8\,\mathrm{m}$ are meshed with $200 \times 80 \times 36$ cells and two additional levels with refinement 2 are used. This corresponds in resolution directly to the level-3 setup from Section 3. To account for establishment of a realistic flow field around the bodies, Car 2 is held in its initial location until $t = 0.25\,\mathrm{s}$. Because of this Car 2 overtakes Car 1 at $t = 0.465955\,\mathrm{s}$.

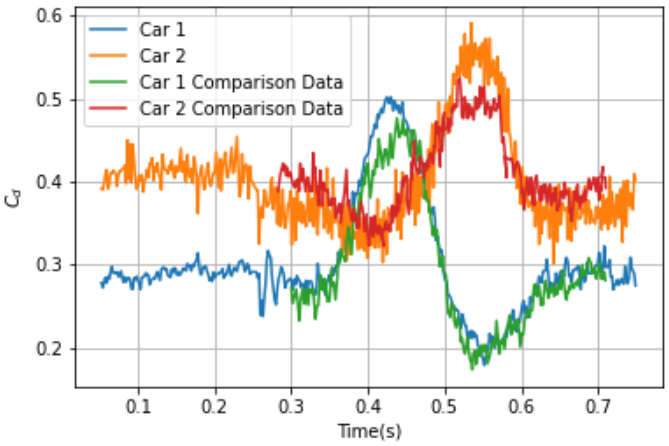

Figure 7: Transient drag coefficients compared to a previous URANS study.

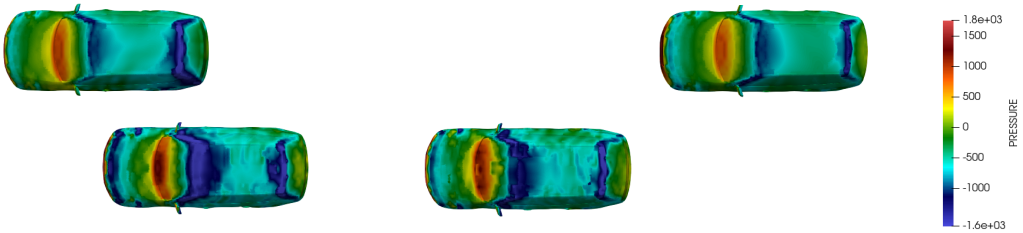

Figure 8: Pressure distributions across Estateback bodies during the overtaking manoeuvrer at $t = 0.416031\,\mathrm{s}$ (left) and $t = 0.5990856\,\mathrm{s}$ (right).

This computation required 4417 time step on level 0 and took $31.8\,\mathrm{h}$ wall time on 160 cores of 2.0 GHz Intel Skylake processors, i.e., $5092\,\mathrm{h}$ CPU.

Figure 7 compares the drag coefficients from AMROC-LBM with the available URANS data. Although the AMROC-LBM run uses the Estateback model, while the comparison data used the Fastback model, the differences are small and can be well explained by the different geometries used. Since it is the only option in StarCCM+ both car's drag coefficients have been computed for $u_0 = 50\,\mathrm{m/s}$ and the slower Car 1 shows initially the lower drag. Car 2 experiences a reduction in drag as it approaches closer to Car 1. Depicting the pressure on the car surfaces in Fig. 8 shows that at $t = 0.416031\,\mathrm{s}$ the lower pressure over Car 2 is skewed towards the side of Car 1, indicating that Car 2 is in the slipstream region of Car 1.

Figure 7 shows that both cars experience a notably increase in drag when leading the other car. Car 1's drag is at a maximum slightly before the cars are parallel and just afterwards Car 2's drag is at a maximum. This is also shown in Fig. 8 as Car 1 has a greater region of low pressure around the region where the boundary layer separates at $t = 0.416031\,\mathrm{s}$ compared to $t = 0.5990856\,\mathrm{s}$. This creates a larger region where there is an adverse pressure gradient and hence an earlier separation of the boundary layer. This induces a larger and more turbulent wake behind the car, increasing its

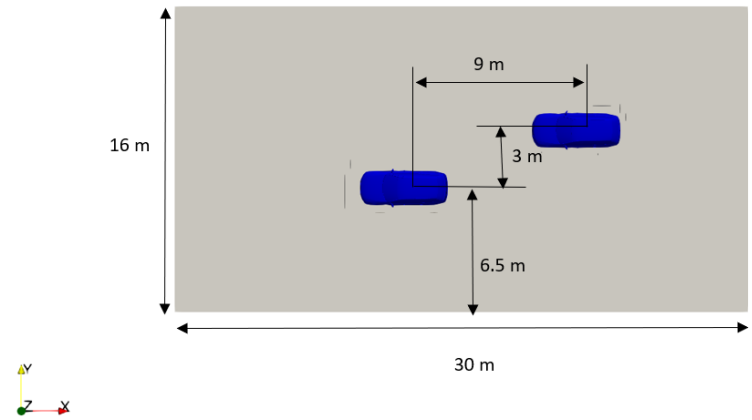

Figure 9: Overhead view of full-scale overtaking setup $t = 0$.

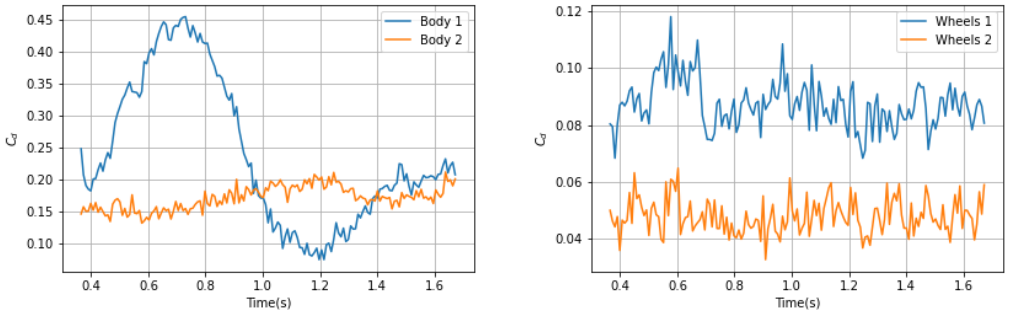

Figure 10: Drag coefficient against time for the body of both models (left) and the wheels of both cars (right).

drag. Since this effect happens to Car 1 when it is leading Car 2 by a small distance, it is concluded that the turbulent air, that is pushed around the side Car 2's body, is directed towards Car 1 and disturbs the flow over the car reducing the flow velocity in the x-direction earlier across the roof and the separation region.

4.2 Full-scale configuration

After verifying the AMROC-LBM methodology in the previous sub-section, a full-scale simulation of two DrivAer Estatebacks is conducted. The inlet flow velocity is again $u_0 = 16\,\mathrm{m/s}$ in the positive x-direction and the relative velocity of the trailing car is set to $10\,\mathrm{m/s}$ moving in the negative direction. The rotating wheel motion is considered for velocities $16\,\mathrm{m/s}$ and $26\,\mathrm{m/s}$, respectively. Figure 9 shows the geometric setup at $t = 0$ with Car 1 being on the left and Car 2 being on the right. A domain of $30\,\mathrm{m} \times 16\,\mathrm{m} \times 7\,\mathrm{m}$ was discretized with a level-0 mesh of $300 \times 160 \times 70$ cells and two additional levels with factor of 2 are used, which corresponds to a finest resolution of $2.5\,\mathrm{cm}$. Approximately 2000 time steps on level 0 were necessary to reach the final displayed time.

The AMROC-LBM setup uses four level set functions to represent the two car

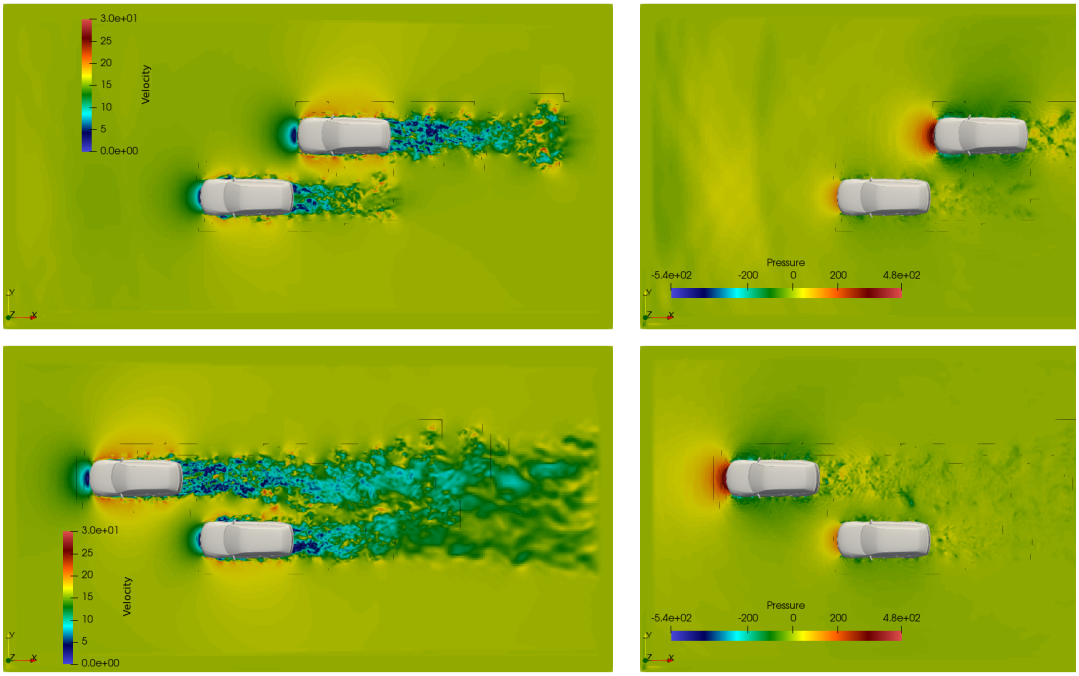

Figure 11: Velocity magnitude (left) and pressure (right) during and after the passage.

bodies and the two wheel sets. In contrast to the verification setup of Section 4.1 the relative motion is started at $t = 0$ and the drag coefficients are calculated with the respective relative flow velocity of each car. Because of this, and the previously explained slip stream effect on the trailing car, the drag coefficients on body and wheel set for Car 2 are actually lower than for Car 1, cf. Fig. 10. Note that shortly before the overtaking the combined drag coefficient on Car 1 is well in agreement with the single car result of Table 1. The observed fluctuations in drag coefficient in Fig. 10 of Car 1 are significantly larger than in Section 4.1, while Car 2 experiences only mild drag coefficient fluctuations due to its considerable higher velocity u_0. Finally, Fig. 11 depicts snapshots of the wake interaction and the pressure fields during the overtaking manoeuvrer.

5 Conclusions

We have demonstrated that our advanced LBM-LES solver AMROC-LBM is capable of accurate vehicle aerodynamic computations for realistic moving geometries. As a final example the overtaking manoeuvre of two DrivAer Estateback cars with rotating wheels with complex spoke geometry is predicted on 160 parallel cores. Key components of AMROC-LBM for this problem class are, beside dynamically adaptive block-structured Cartesian meshing, an advanced lattice-Boltzmann a scheme, LES modelling with the dynamic Smagorinsky approach and a wall function model to incorporate the intrinsically turbulent boundary layers around the car geometries.

Although the contribution is small for this configuration, cf. Table 2, future work will improve the accuracy of this solver by considering the eddy viscosity modification of Eq. (11) in the viscous stress evaluation and also allow deactivation of the wall function model in case of an adverse pressure gradient at the wall.

References

[1] M. Grondeau, R. Deiterding, "Direct prediction of flow noise around airfoils using an adaptive lattice Boltzmann method", in B. Stoevesandt, G. Schepers, P. Fuglsang, S. Yuping (Editors), Handbook of Wind Energy Aerodynamics, Springer, 2021.

[2] J. Latt, B. Chopard, "Lattice Boltzmann method with regularized pre-collision distribution functions", Mathematics and Computers in Simulation, 72, 165–168, 2006.

[3] O. Malaspinas, "Increasing stability and accuracy of the lattice Boltzmann scheme: recursivity and regularization", 2015.

[4] R. Deiterding, "Block-structured adaptive mesh refinement - theory, implementation and application", European Series in Applied and Industrial Mathematics: Proceedings, 34, 97–150, 2011.

[5] R. Deiterding, S.L. Wood, "An adaptive lattice Boltzmann method for predicting wake fields behind wind turbines", in A. Dillmann, G. Heller, E. Krämer, C. Wagner, C. Breitsamter (Editors), New Results in Numerical and Experimental Fluid Mechanics X, Volume 132, pages 845–857. Springer, 2016.

[6] A. Dupuis, B. Chopard, "Theory and applications of an alternative lattice Boltzmann grid refinement algorithm", Physical Review E, 67(6), 066707, 2003.

[7] J. Smagorinsky, "General circulation experiments with the primitive equations", Monthly Weather Review, 91(3), 99–163, 1963.

[8] M. Germano, U. Piomelli, P. Moin, W.H. Cabot, "A dynamic subgrid-scale eddy viscosity model", Phys. Fluids A, 3(7), 1760–1765, 1991.

[9] O. Malaspinas, P. Sagaut, "Consistent subgrid scale modelling for lattice Boltzmann methods", Journal of Fluid Mechanics, 700, 514–542, 2012.

[10] Z. Guo, C. Zheng, B. Shi, "An extrapolation method for boundary conditions in lattice Boltzmann method", Physics of Fluids, 14(6), 2007–2010, 2002-06.

[11] E.W.S. Kam, R.M.C. So, R.C.K. Leung, "Lattice Boltzman Method Simulation of Aeroacoustics and Nonreflecting Boundary Conditions", AIAA Journal, 45 (7), 1703–1712, 2007-07.

[12] A.J. Musker, "Explicit Expression for the Smooth Wall Velocity Distribution in a Turbulent Boundary Layer", AIAA Journal, 17(6), 655–657, 1979.

[13] A.I. Heft, T. Indiger, N.A. Adams, "Introduction of a new realistic generic car model for aerodynamic investigations", Technical Report 2012-01-0168, SAE Technical Paper, 2012.

[14] B. Hanschke, R. Deiterding, Technical report, German Aerospace Center (DLR), Dec 2014.